Proceedings of the
Annual Stability Conference
Structural Stability Research Council
St. Louis, Missouri, April 2-5, 2019

Uncertainties in Seismic Collapse Analysis of Framed Structures

Kevin K.F. Wong[1]

Abstract

Can small-displacement-based solution algorithms be used to predict large displacement responses, such as at collapse or near-collapse? Framed structures often experience large displacement with significant nonlinear response prior to collapse. To capture the nonlinearity in structural response, both geometric and material nonlinearities must be considered in the analysis. The implementation of geometric and material nonlinearities in solution algorithms among various software packages is not treated consistently, where different assumptions are made in the formulations without the users' knowledge. For example, large-displacement-based solution algorithms use finite element formulations that update geometry at every time step, which is significantly different from other structural analysis solution algorithms that use small displacement theory with constant geometric stiffness matrix. These different assumptions introduce levels of uncertainty in the structural response prediction, especially when one solution algorithm predicts structural collapse while another solution algorithm predicts that the structure remains standing. To quantify these uncertainties associated with different small-displacement-based solution algorithms, this research investigates the dynamic instability of framed structures by quantitatively comparing the responses predicted among the associated software packages with a large-displacement-based software package that is more capable of predicting large displacement responses. The focus is placed on how each software package implements geometric nonlinearity for analyzing steel framed structures. Comparing the simulated response history results shows that the mean percentage differences between small-displacement-based and large-displacement-based solution algorithms range from 10 % to 30 % at near-collapse based on the use of seven earthquake ground motions. The outcome of this research provides insights to questions that have often been raised in terms of the precision of small-displacement-based solution algorithms in predicting large displacement response and structural collapse.

1. Introduction

Performance-based seismic engineering is a useful tool for designing new structures and improving the seismic performance of existing structures. Modeling of these structures and simulation of responses for determining the seismic demands up to collapse is an essential part of the engineering process. While the seismic demands are compared with the corresponding seismic capacity in design, the analysis behind the process for determining the seismic demands

[1] Research Structural Engineer, National Institute of Standards and Technology, <kfwong@nist.gov>

may be sensitive to the software package and the associated solution algorithm used to conduct the analysis. Many of the seismic analysis solution algorithms used today employ small-displacement theory to solve a wide-variety of nonlinear structural dynamic problems, up to and including structural collapse. Examples of using small-displacement-based software packages to solve collapse problems in recent years can be found for steel structures (Guo *et al*. 2015, Tirca *et al*. 2015, Fathieh and Mercan 2016, Wang *et al*. 2017), concrete structures (Arabzadeh and Galal 2017, Mulas and Martinelli 2017), and wood structures (Pang and Shirazi 2013).

Being able to capture structural collapse or near collapse requires software packages to handle significant coupling between geometric and material nonlinearities. Since steel structures are more susceptible to the adverse effects from geometric nonlinearity due to the use of slender members, most research has been focused on understanding the collapse behavior of these structures, especially for moment-resisting frames (Lignos *et al*. 2011, Grigorian and Grigorian 2012, Eads *et al*. 2013, Domizio *et al*. 2015); these studies are all based on results obtained using small-displacement-based solution algorithms. These software packages, either commercially available or research-oriented, have typically been developed to give reasonable results when analyzing models with material nonlinearities and separately when analyzing models with geometric nonlinearities. However, the complexity of nonlinear analysis can lead to inconsistent results when the analysis requires significant coupling between geometric and material nonlinearities. This coupling between yielding components for material nonlinearity and member stability for geometric nonlinearity makes the problem difficult to solve, and therefore addressing this nonlinear coupling in solution algorithms remains a challenge.

This paper presents recent research concerning the evaluation of several small-displacement-based software packages based on various geometric nonlinearity and material nonlinearity formulations to understand how each solution algorithm handles the coupling to capture large-displacement structural dynamic responses up to collapse. Numerical simulations are performed to simulate the nonlinear structural dynamic responses of an eight-story steel moment-resisting frame based on four different geometric nonlinearity formulations of small-displacement-based solution algorithms. The simulated responses are compared with those obtained using a large-displacement-based finite element analysis software package. Through this study, the applicability and limitations of using small-displacement-based software packages in simulating large displacement responses and structural collapse are examined with uncertainties quantified.

2. Small-Displacement-Based Stiffness Matrix for Geometric and Material Nonlinearities

The original theory of incorporating geometric nonlinearity based on small displacement was first developed for elastic columns in the 1960's (Timoshenko and Gere 1961, Bazant and Cedolin 2003) without any consideration of yielding and formation of plastic hinge. But it found limited application because of its complexity in the closed-form solution as compared to those methods of using either the P-Δ stiffness approach (Powell 2010) or the geometric stiffness approach (Wilson 2010). However, when large lateral deflections in framed structures are expected, excessive geometric nonlinearity is coupled with excessive material nonlinearity, and the first-order or second-order approximation of the geometric nonlinearity may not be able to capture the nonlinear behavior accurately. Therefore, the original theory that included geometric nonlinearity is rederived here with the incorporation of material nonlinearity. This is done by using a column member with plastic hinges at both ends and subjected to a compressive force.

Here, four degrees of freedom (DOFs) and two plastic hinge locations (PHLs) are used to describe the movements at the two ends of a column member in a moment-resisting frame. These movements at the two ends include lateral displacement ($v(0)$ and $v(L)$), rotation ($v'(0)$ and $v'(L)$), and plastic rotations at the two plastic hinges (θ_a'' and θ_b''). To compute the member stiffness matrix $\mathbf{k}_i$, each of these 4 DOFs and 2 PHLs is displaced independently by one unit as shown in Fig. 1 while subjected to an axial compressive load P. Here, V_{1s}, M_{1s}, V_{2s}, and M_{2s} represent the required shear forces and moments at the two ends of the member to cause the prescribed pattern, where $s = 1, \ldots, 6$ represents the six cases of unit displacement patterns of the member's movements, and M_{as} and M_{bs} represent the moment at plastic hinges 'a' and 'b', respectively, due to the prescribed pattern. Note that subscript '1' denotes the near end and subscript '2' denotes the far end for the calculated shears and moments. Therefore, the '1' end coincides with plastic hinge 'a' and the '2' end coincides with plastic hinge 'b'.

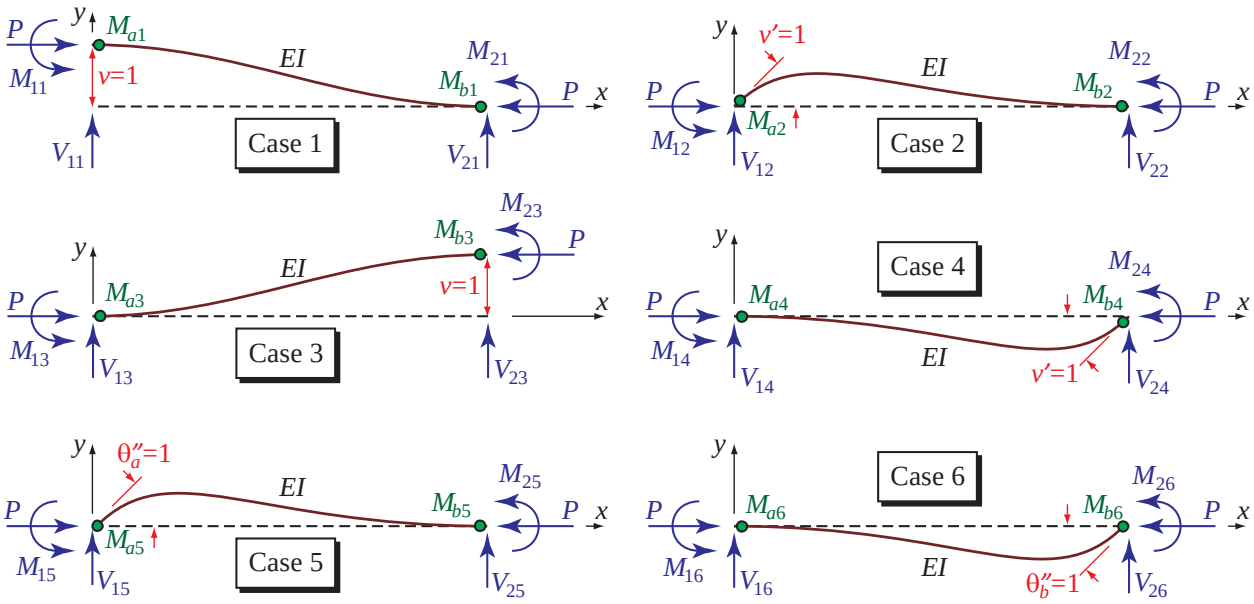

Figure 1: Six cases of unit displacement patterns and the corresponding fixed-end forces and hinge moments

Using the classical Bernoulli-Euler beam theory with homogeneous and isotropic material properties, where the moment is proportional to the curvature and plane sections are assumed to remain plane based on small displacements, the governing equilibrium equation describing the deflected shape of the member can be written as

$$(EIv'')'' + Pv'' = 0 \tag{1}$$

where E is the elastic modulus, I is the moment of inertia, v is the lateral deflection, P is the axial compressive force on the member, and each prime represents taking derivatives of the corresponding variable with respect to the x-direction of the member. By assuming EI is constant along the member, the solution to the fourth-order ordinary differential equation given in Eq. 1 becomes:

$$v = A\sin kx + B\cos kx + Cx + D \tag{2}$$

where $k^2 = P/EI$ and *A*, *B*, *C*, and *D* are constants to be determined by imposing different boundary conditions. Let $\lambda = kL$ to simplify the derivations, where *L* is the length of the member. The following cases of boundary conditions are now considered. Note that Cases 3 and 4 are first derived because of their simplicity in the solutions to the differential equation.

2.1 Case 4

For Case 4 as shown in Fig. 1, imposing the boundary conditions $v(0) = 0$, $v'(0) = 0$, $v(L) = 0$, $v'(L) = 1$, and $\theta_a'' = \theta_b'' = 0$ on Eq. 2 gives

$$v(0) = 0: \qquad B + D = 0 \tag{3a}$$
$$v'(0) = 0: \qquad kA + C = 0 \tag{3b}$$
$$v(L) = 0: \qquad A\sin\lambda + B\cos\lambda + CL + D = 0 \tag{3c}$$
$$v'(L) = 1: \qquad kA\cos\lambda - kB\sin\lambda + C = 1 \tag{3d}$$

Solving simultaneously for the constants in Eq. 3 gives

$$A = \frac{L(1-\cos\lambda)}{\lambda(\lambda\sin\lambda + 2\cos\lambda - 2)} \quad , \quad B = \frac{L(\sin\lambda - \lambda)}{\lambda(\lambda\sin\lambda + 2\cos\lambda - 2)} \quad , \quad C = -kA \quad , \quad D = -B \tag{4}$$

Therefore, Eq. 2 along with the constants in Eq. 4 gives the deflected shape for Case 4. The shears (i.e., V_{14} and V_{24}) and moments (i.e., M_{14} and M_{24}) at the two ends of the member (see Fig. 1) are then evaluated using the classical Bernoulli-Euler beam theory formula:

$$M(x) = EIv'' \quad , \quad V(x) = EIv''' + Pv' \tag{5}$$

Now taking derivatives of Eq. 2 and substituting the results into Eq. 5 while using the constants calculated in Eq. 4, the shears and moments at the two ends of the member (i.e., the four DOFs) for Case 4 in Fig. 1 are calculated as:

$$M_{14} = -EIv''(0) = EIk^2 B = \hat{s}\hat{c}EI/L \tag{6a}$$
$$V_{14} = EIv'''(0) + Pv'(0) = -EIk^3 A + P \times 0 = \bar{s}EI/L^2 \tag{6b}$$
$$M_{24} = EIv''(L) = -EIk^2(A\sin\lambda + B\cos\lambda) = \hat{s}EI/L \tag{6c}$$
$$V_{24} = -EIv'''(L) - Pv'(L) = EIk^3(A\cos\lambda - B\sin\lambda) - P \times 1 = -\bar{s}EI/L^2 \tag{6d}$$

where $\hat{s}$, $\hat{c}$, and $\bar{s}$ are the stability coefficients computed by the formula

$$\hat{s} = \frac{\lambda(\sin\lambda - \lambda\cos\lambda)}{2 - 2\cos\lambda - \lambda\sin\lambda} \quad , \quad \hat{c} = \frac{\lambda - \sin\lambda}{\sin\lambda - \lambda\cos\lambda} \quad , \quad \bar{s} = \hat{s} + \hat{s}\hat{c} = \frac{\lambda^2(1-\cos\lambda)}{2 - 2\cos\lambda - \lambda\sin\lambda} \tag{7}$$

The minus signs appear in front of the equations for M_{14} in Eq. 6a and V_{24} in Eq. 6d because there is a difference in sign convention between the classical Bernoulli-Euler beam theory and the theory for the stiffness method of structural analysis.

Finally, the moments at the two PHLs can be evaluated by recognizing that these moments must equal to the end moments by equilibrium, i.e., $M_{a4} = M_{14}$ and $M_{b4} = M_{24}$. Therefore,

$$M_{a4} = M_{14} = \hat{s}\hat{c}EI/L \quad , \quad M_{b4} = M_{24} = \hat{s}EI/L \tag{8}$$

2.2 Case 3

For Case 3 as shown in Fig. 1, imposing the boundary conditions $v(0) = 0$, $v'(0) = 0$, $v(L) = 1$, $v'(L) = 0$, and $\theta_a'' = \theta_b'' = 0$ on Eq. 2 gives

$$v(0) = 0: \qquad B + D = 0 \tag{9a}$$
$$v'(0) = 0: \qquad kA + C = 0 \tag{9b}$$
$$v(L) = 1: \qquad A\sin\lambda + B\cos\lambda + CL + D = 1 \tag{9c}$$
$$v'(L) = 0: \qquad kA\cos\lambda - kB\sin\lambda + C = 0 \tag{9d}$$

Solving simultaneously for the constants in Eq. 9 gives

$$A = -\frac{\sin\lambda}{\lambda\sin\lambda + 2\cos\lambda - 2} \quad , \quad B = \frac{1-\cos\lambda}{\lambda\sin\lambda + 2\cos\lambda - 2} \quad , \quad C = -kA \quad , \quad D = -B \tag{10}$$

These constants in Eq. 10 are used to give the deflected shape in Eq. 2 for Case 3. Now substituting Eq. 2 into Eq. 5 and using the constants calculated in Eq. 10, the shears and moments at the four DOFs for Case 3 in Fig. 1 are calculated as:

$$M_{13} = -EIv''(0) = EIk^2 B = -\bar{s}EI/L^2 \tag{11a}$$
$$V_{13} = EIv'''(0) + Pv'(0) = -EIk^3 A + P\times 0 = -s'EI/L^3 \tag{11b}$$
$$M_{23} = EIv''(L) = -EIk^2\left(A\sin\lambda + B\cos\lambda\right) = -\bar{s}EI/L^2 \tag{11c}$$
$$V_{23} = -EIv'''(L) - Pv'(L) = EIk^3\left(A\cos\lambda - B\sin\lambda\right) - P\times 0 = s'EI/L^3 \tag{11d}$$

where s' is the fourth and final stability coefficient given by the formula

$$s' = 2\bar{s} - \lambda^2 = \frac{\lambda^3\sin\lambda}{2 - 2\cos\lambda - \lambda\sin\lambda} \tag{12}$$

Finally, the moments at the two PHLs are evaluated by equilibrium as

$$M_{a3} = M_{13} = -\bar{s}EI/L^2 \quad , \quad M_{b3} = M_{23} = -\bar{s}EI/L^2 \tag{13}$$

2.3 Case 2

For Case 2 as shown in Fig. 1, by imposing the boundary conditions $v(0) = 0$, $v'(0) = 1$, $v(L) = 0$, $v'(L) = 0$, and $\theta_a'' = \theta_b'' = 0$ on Eq. 2, solution can be obtained via the same procedure presented above while solving for a different set of constants. On the other hand, a more direct solution can be obtained by recognizing that Case 2 is exactly the same as 'rotating' Case 4 by 180°. Doing so, the solution becomes

$$V_{12} = -V_{24} = \bar{s}EI/L^2 \quad , \quad V_{22} = -V_{14} = -\bar{s}EI/L^2 \tag{14a}$$

$$M_{12} = M_{24} = \hat{s}EI/L \quad , \quad M_{22} = M_{14} = \hat{s}\hat{c}EI/L \tag{14b}$$

$$M_{a2} = M_{b4} = \hat{s}EI/L \quad , \quad M_{b2} = M_{a4} = \hat{s}\hat{c}EI/L \tag{14c}$$

2.4 Case 1

For Case 1 as shown in Fig. 1, by imposing the boundary conditions $v(0) = 1$, $v'(0) = 0$, $v(L) = 0$, $v'(L) = 0$, and $\theta_a'' = \theta_b'' = 0$ on Eq. 2, solution can be obtained via the same procedure presented above while solving for a different set of constants. On the other hand, a more direct solution can be obtained by recognizing that Case 1 is exactly the same as 'flipping' Case 3 by 180°. Doing so, the solution becomes

$$V_{11} = V_{33} = s'EI/L^3 \quad , \quad V_{21} = V_{13} = -s'EI/L^3 \tag{15a}$$

$$M_{11} = -M_{23} = \bar{s}EI/L^2 \quad , \quad M_{21} = -M_{13} = \bar{s}EI/L^2 \tag{15b}$$

$$M_{a1} = -M_{b3} = \bar{s}EI/L^2 \quad , \quad M_{b1} = -M_{a3} = \bar{s}EI/L^2 \tag{15c}$$

2.5 Case 5

For Case 5 as shown in Fig. 1, by imposing the boundary conditions $\theta_a'' = 1$, $\theta_b'' = 0$, and $v(0) = v'(0) = v(L) = v'(L) = 0$ on Eq. 2, solution can be obtained via direct comparison of Case 2 and Case 5, where a unit plastic rotation at hinge '*a*' gives the same displacement pattern as a unit rotation at the '1' end. It follows that the forces and moments at the four DOFs and two PHLs are the same for both cases, i.e.,

$$V_{1a} = V_{12} = \bar{s}EI/L^2 \quad , \quad V_{2a} = V_{22} = -\bar{s}EI/L^2 \tag{16a}$$

$$M_{1a} = M_{12} = \hat{s}EI/L \quad , \quad M_{2a} = M_{22} = \hat{s}\hat{c}EI/L \tag{16b}$$

$$M_{aa} = M_{a2} = \hat{s}EI/L \quad , \quad M_{ba} = M_{b2} = \hat{s}\hat{c}EI/L \tag{16c}$$

2.6 Case 6

Finally, for Case 6 as shown in Fig. 1, by imposing the boundary conditions $\theta_a'' = 0$, $\theta_b'' = 1$, and $v(0) = v'(0) = v(L) = v'(L) = 0$ on Eq. 2, solution can be obtained via direct comparison of Case 4 and Case 6, where a unit plastic rotation at hinge '*b*' gives the same displacement pattern as a unit rotation at the '2' end. It follows that the forces and moments at the four DOFs and two PHLs are the same for both cases, i.e.,

$$V_{1b} = V_{14} = \bar{s}EI/L^2 \quad , \quad V_{2b} = V_{24} = -\bar{s}EI/L^2 \tag{17a}$$

$$M_{1b} = M_{14} = \hat{s}\hat{c}EI/L \quad , \quad M_{2b} = M_{24} = \hat{s}EI/L \tag{17b}$$

$$M_{ab} = M_{a4} = \hat{s}\hat{c}EI/L \quad , \quad M_{bb} = M_{b4} = \hat{s}EI/L \tag{17c}$$

2.7 Stiffness Matrices

In summary, based on Eqs. 6, 8, 11, and 11-17 for the above six cases, the small-displacement-based member stiffness matrix of the i^{th} member $\mathbf{k}_i^{SF}$ for bending becomes

$$\mathbf{k}_i^{SF} = \frac{EI}{L^3}\left[\begin{array}{cccc:cc} s' & \bar{s}L & -s' & \bar{s}L & \bar{s}L & \bar{s}L \\ \bar{s}L & \hat{s}L^2 & -\bar{s}L & \hat{s}\hat{c}L^2 & \hat{s}L^2 & \hat{s}\hat{c}L^2 \\ -s' & -\bar{s}L & s' & -\bar{s}L & -\bar{s}L & -\bar{s}L \\ \bar{s}L & \hat{s}\hat{c}L^2 & -\bar{s}L & \hat{s}L^2 & \hat{s}\hat{c}L^2 & \hat{s}L^2 \\ \hdashline \bar{s}L & \hat{s}L^2 & -\bar{s}L & \hat{s}\hat{c}L^2 & \hat{s}L^2 & \hat{s}\hat{c}L^2 \\ \bar{s}L & \hat{s}\hat{c}L^2 & -\bar{s}L & \hat{s}L^2 & \hat{s}\hat{c}L^2 & \hat{s}L^2 \end{array}\right] \begin{array}{l} \leftarrow v(0) \\ \leftarrow v'(0) \\ \leftarrow v(L) \\ \leftarrow v'(L) \\ \leftarrow \theta_a'' \\ \leftarrow \theta_b'' \end{array} \tag{18}$$

where the superscript '*SF*' is used to denote that the member stiffness matrix $\mathbf{k}_i$ is obtained by using the stability functions method that is computed based on the stability coefficients $\hat{s}$, $\hat{c}$, and $\bar{s}$ in Eq. 7 and s' in Eq. 12.

Linearization of Eq. 18 can be performed by using Taylor series expansion on each term of the member stiffness matrix and truncating higher-order terms. Doing so gives

$$\mathbf{k}_i^{GS} = \frac{EI}{L^3}\begin{bmatrix} 12 & 6L & -12 & 6L \\ 6L & 4L^2 & -6L & 2L^2 \\ -12 & -6L & 12 & -6L \\ 6L & 2L^2 & -6L & 4L^2 \end{bmatrix} - \begin{bmatrix} 6P/5L & P/10 & -6P/5L & P/10 \\ P/10 & 2PL/15 & -P/10 & -PL/30 \\ -6P/5L & -P/10 & 6P/5L & -P/10 \\ P/10 & -PL/30 & -P/10 & 2PL/15 \end{bmatrix} \begin{array}{l} \leftarrow v(0) \\ \leftarrow v'(0) \\ \leftarrow v(L) \\ \leftarrow v'(L) \end{array} \tag{19}$$

where the first matrix in Eq. 19 represents that classic stiffness matrix without considering any geometric nonlinearity, and the second matrix represents the geometric stiffness. The superscript '*GS*' is used to denote that the member stiffness matrix $\mathbf{k}_i$ is computed by using the geometric stiffness method. Note that the member stiffness matrices in Eq. 19 are 4×4 matrices, where the rows and columns associated with θ_a'' and θ_b'' are dropped. This is because solution algorithms among various software packages that incorporate geometric nonlinearity using the geometric stiffness method usually adopt a different and independent algorithm for material nonlinearity.

Finally, the member stiffness matrix in Eq. 20 can be further simplified by retaining only the large *P*-Δ effect while ignoring the small *P*-δ effect. This is done by removing all the geometric nonlinear terms associated with bending. Doing so gives

$$\mathbf{k}_i^{PD} = \frac{EI}{L^3}\begin{bmatrix} 12 & 6L & -12 & 6L \\ 6L & 4L^2 & -6L & 2L^2 \\ -12 & -6L & 12 & -6L \\ 6L & 2L^2 & -6L & 4L^2 \end{bmatrix} - \begin{bmatrix} P/L & 0 & -P/L & 0 \\ 0 & 0 & 0 & 0 \\ -P/L & 0 & P/L & 0 \\ 0 & 0 & 0 & 0 \end{bmatrix} \begin{array}{l} \leftarrow v(0) \\ \leftarrow v'(0) \\ \leftarrow v(L) \\ \leftarrow v'(L) \end{array} \tag{20}$$

where the superscript '*PD*' is used to denote that the member stiffness matrix $\mathbf{k}_i$ is computed by using the *P*-Δ stiffness method.

3. Structural Model

To investigate the coupling effects of geometric nonlinearity and material nonlinearity on the structural dynamic responses among solution algorithms, consider an eight-story, three-bay steel

moment-resisting frame as shown in Fig. 2a. The structural model of this frame consists of 8 lateral degrees of freedom (DOFs) and 112 plastic hinge locations (PHLs) as shown in the figure. Let the mass be 74 075 kg on each floor. No leaning column is used in the analytical model in order to accommodate some limitations in certain solution algorithms, and therefore gravity loads acting on the frame have been slightly magnified to reflect the additional gravity load that would have otherwise been acting on the leaning column. The magnified gravity load is shown in Fig. 2b, and geometric nonlinearity of the columns is considered due to this gravity load. The resulting initial periods (without consideration of geometric nonlinearity by setting $P = 0$ in Eq. 19 or 20) and elastic periods (with consideration of geometric nonlinearity due to gravity loads based on the member stiffness formulation in Eq. 18) for the eight modes of vibration, labeled as T1 to T8, are summarized in Table 1. Assume all 112 plastic hinges exhibit elastic-plastic behavior to eliminate the differences in simulated responses caused by different implementation of hardening and strength loss rules in the solution algorithms. All plastic hinges are assumed to have 152 mm offset from the center of the beam-column connection, and panel zones are not modeled to simplify the analysis. Let the elastic modulus be 200 GPa and yield stress of steel be 345 MPa for all members. A detailed explanation of the structural model for the implementation of each solution algorithm is discussed in the following subsections.

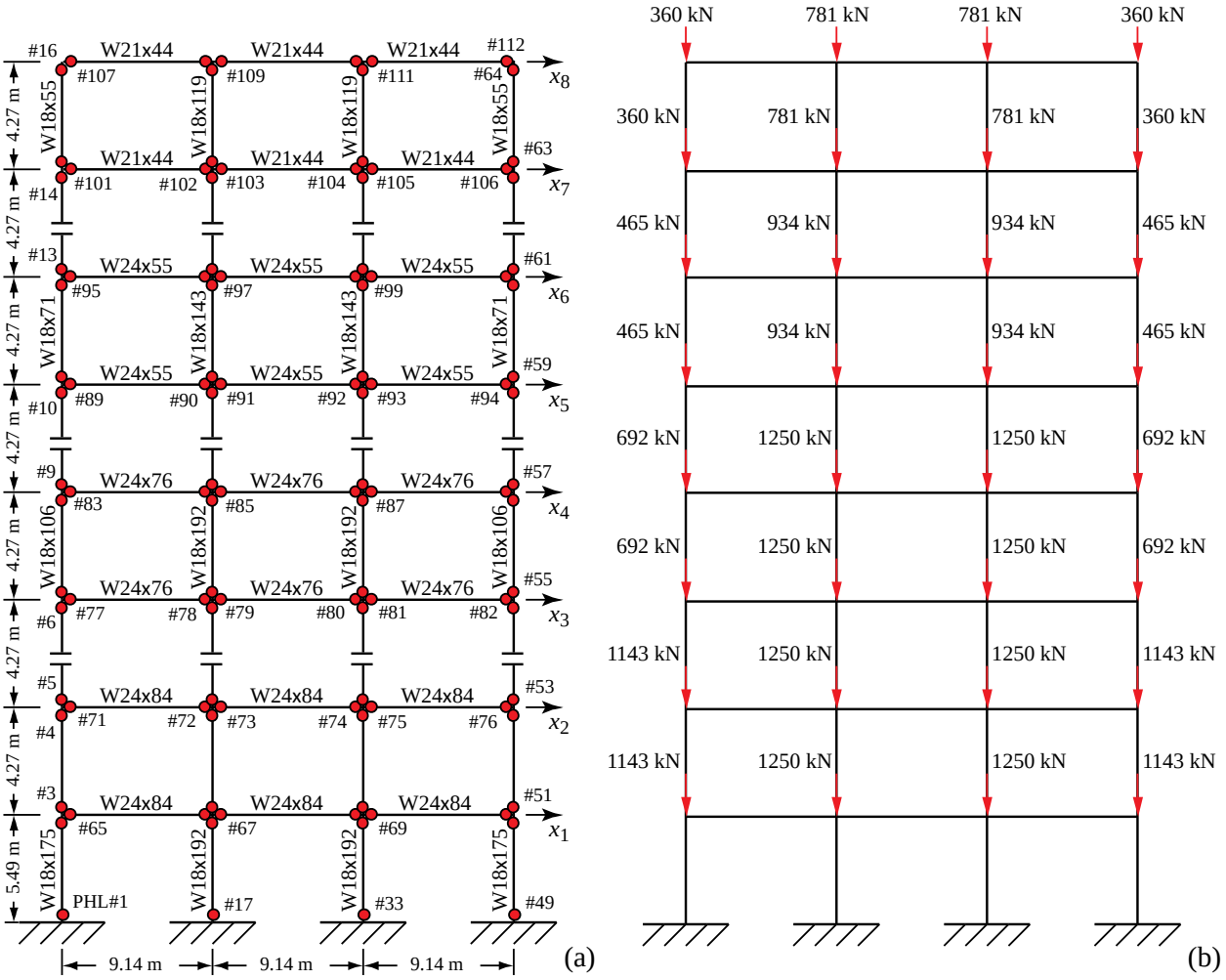

Figure 2: Eight-story three-bay steel moment frame with gravity loads

Table 1: Periods of vibration using different stiffness representations of the eight-story frame

Stiffness	T1	T2	T3	T4	T5	T6	T7	T8
Initial	1.70 s	0.62 s	0.34 s	0.22 s	0.16 s	0.12 s	0.10 s	0.08 s
Elastic	1.81 s	0.65 s	0.36 s	0.23 s	0.16 s	0.12 s	0.10 s	0.08 s

3.1 A Small-Displacement-Based Algorithm Using P-Delta Stiffness Formulation (PD)

The investigated PD solution algorithm is embedded in a commercial nonlinear structural analysis software package that is commonly used in professional practice to perform nonlinear static and dynamic analyses. For this reason, various features have been automatically included in the model development to simplify the input process, such as elastic shear deformation and yielding of column plastic hinges due to axial force and moment interactions. Including shear deformations in the structural model reduces the initial stiffness that is based on flexure only, and therefore the mass on each floor of the frame is reduced to 69 487 kg (a 6.2 % reduction) to give consistent periods of vibration of the frame as summarized in Table 1. In addition, this PD solution algorithm uses the P-Delta stiffness formulation presented in Eq. 20 that considers only large P-Δ effects while ignoring small P-δ effects. The target for damping is to achieve a Rayleigh damping having a mass proportional constant of 0.25 and a stiffness proportional constant of 0.0. However, because the PD solution algorithm automatically adds numerical damping to the analysis when geometric nonlinearity is considered, the damping constants are calibrated and scaled down in this case such that Rayleigh damping with mass proportional constant of 0.2132 and a stiffness proportional constant of 0.0 is used in the model.

3.2 A Small-Displacement-Based Algorithm Using Geometric Stiffness Formulation (GS)

The investigated GS solution algorithm is embedded in a commercial nonlinear structural analysis software package that is commonly used in professional practice to perform structural design. For this reason, various features have also been automatically included in the model development to simplify the input process, such as elastic shear deformation. However, including shear deformations in the structural model reduces the initial stiffness that is based on flexure only, and therefore the shear area of the model is intentionally set to zero in order to give consistent periods of vibration of the frame as summarized in Table 1. In addition, this GS solution algorithm uses geometric stiffness formulation presented in Eq. 19 that considers both large P-Δ and small P-δ effects. Rayleigh damping having a mass proportional constant of 0.25 and a stiffness proportional constant of 0.0 is used. Lumped plasticity is selected to model the yielding of plastic hinges, but the GS solution algorithm allows only the yield moment as input without consideration of axial force and moment interaction. In order to match the yielding characteristics of GS with those defined in PD, the yield moments of the plastic hinges are therefore adjusted accordingly based on the column axial forces from gravity loads.

3.3 A Small-Displacement-Based Algorithm Based on Stability Functions Formulation (SF)

The investigated SF solution algorithm is based on the nonlinear structural dynamic analysis theory to address material nonlinearity in a dynamic context (Li and Wong 2014) and uses the stability functions formulation presented in Eq. 18 with both large P-Δ and small P-δ effects included for the geometric nonlinearity formulation. This algorithm requires damping inputs be in the form of modal damping, where the periods of vibration are based on the elastic stiffness of the frame as shown in Table 1. To achieve the target of Rayleigh damping having a mass proportional constant of 0.25 and a stiffness proportional constant of 0.0, the damping ratios are calculated by performing eigenvalue and eigenvector analyses and found to be 3.41 %, 1.22 %,

0.67 %, 0.43 %, 0.31 %, 0.23 %, 0.18 %, and 0.15 % among the eight modes of vibration. The material nonlinearity options of the SF solution algorithm are the least sophisticated among all the algorithms used in this study. Only a bilinear backbone curve with kinematic hardening is available for the model with a pre-defined yield moment. Therefore, in order for the yielding characteristics of the model to be compatible with those defined in PD, the yield moments of the plastic hinges are computed based on the column axial forces due to the gravity loads, which is similar to the computation performed for the GS solution algorithm.

3.4 A Small-Displacement-Based Algorithm Based on Corotation Formulation (CR)

The investigated CR solution algorithm is embedded in a research-oriented nonlinear structural analysis software package. This algorithm provides the option to choose between the P-Delta stiffness formulation or the corotation formulation (Belytschko and Hsieh 1973, Sivaselvan and Reinhorn 2002) that considers large rigid-body displacement with small strains, both of which considers only large P-Δ effects while ignoring small P-δ effects. The corotation formulation has been selected for this study to investigate whether large rigid body displacement is needed for the nonlinear analysis of structure that is fixed to the ground. This CR solution algorithm takes Rayleigh damping as inputs, and therefore Rayleigh damping having a mass proportional constant of 0.25 and a stiffness proportional constant of 0.0 is used. Lumped plasticity is selected to model the yielding of plastic hinges, but similar to the GS and SF solution algorithms it allows only the yield moment as input without consideration of axial force and moment interaction. In order to match the yielding characteristics of CR with those defined of PD, the yield moments of the plastic hinges are therefore computed based on the column axial forces from gravity loads.

3.5 A Large-Displacement-Based Algorithm Using Large Displacement Formulation (LD)

The investigated LD solution algorithm is embedded in a commercial finite element analysis software package that is based on a large displacement formulation (Belytschko and Liu 2014, Reddy 2015). This formulation expresses equilibrium in its deformed state that can couple with significant inelastic deformation, thereby capturing both geometric nonlinearity and material nonlinearity in every element. The drawback is that each member must be subdivided into many finite elements to capture the displacement profile. In the structural model, 10 elements are used to model each column member and 18 elements used to model each beam member, resulting in a significant increase in computational efforts. This LD solution algorithm takes Rayleigh damping as inputs, and therefore Rayleigh damping having a mass proportional constant of 0.25 and a stiffness proportional constant of 0.0 is used. For the yielding of plastic hinges, the interaction between the axial force and moments is considered at the integration points of the cross-section of each element, and therefore the yield stress for the members must be calibrated to match the yielding characteristics used in PD, GS, SF, and CR. The yield stress for beams are calibrated to 354 MPa for having no interaction with the axial force P, while the yield stresses for columns are calibrated at every two floors. These calibrated yield stresses are 365 MPa, 379 MPa, 386 MPa, and 400 MPa, respectively, from the columns at the bottom two floors up to the columns at the top two floors.

3.6 Summary

Table 2 summarizes the different modeling techniques used among the five solution algorithms (PD, GS, SF, CR, and LD) for developing consistent models of the eight-story frame shown in Fig. 2.

Table 2: Modeling techniques among each solution algorithms

	PD	GS	SF	CR	LD
Geometric Nonlinearity	P-Delta Stiffness	Geometric Stiffness	Stability Functions	Corotation	Finite Element
Damping	Rayleigh	Rayleigh	Modal	Rayleigh	Rayleigh
Shear Deformation	Yes	No	No	No	Yes
Material Nonlinearity	*P-M* interaction	Moment at *P* due to Gravity	Moment at *P* due to Gravity	Moment at *P* due to Gravity	Yield Stress at Integration Points

4. Nonlinear Response History Analyses

A total of 7 earthquake ground motions is used to excite the eight-story frame in Fig. 2, and these ground motion time histories are presented in Fig. 3. Various scaling factors are used to intensify each earthquake ground motion to cause collapses among the five solution algorithms.

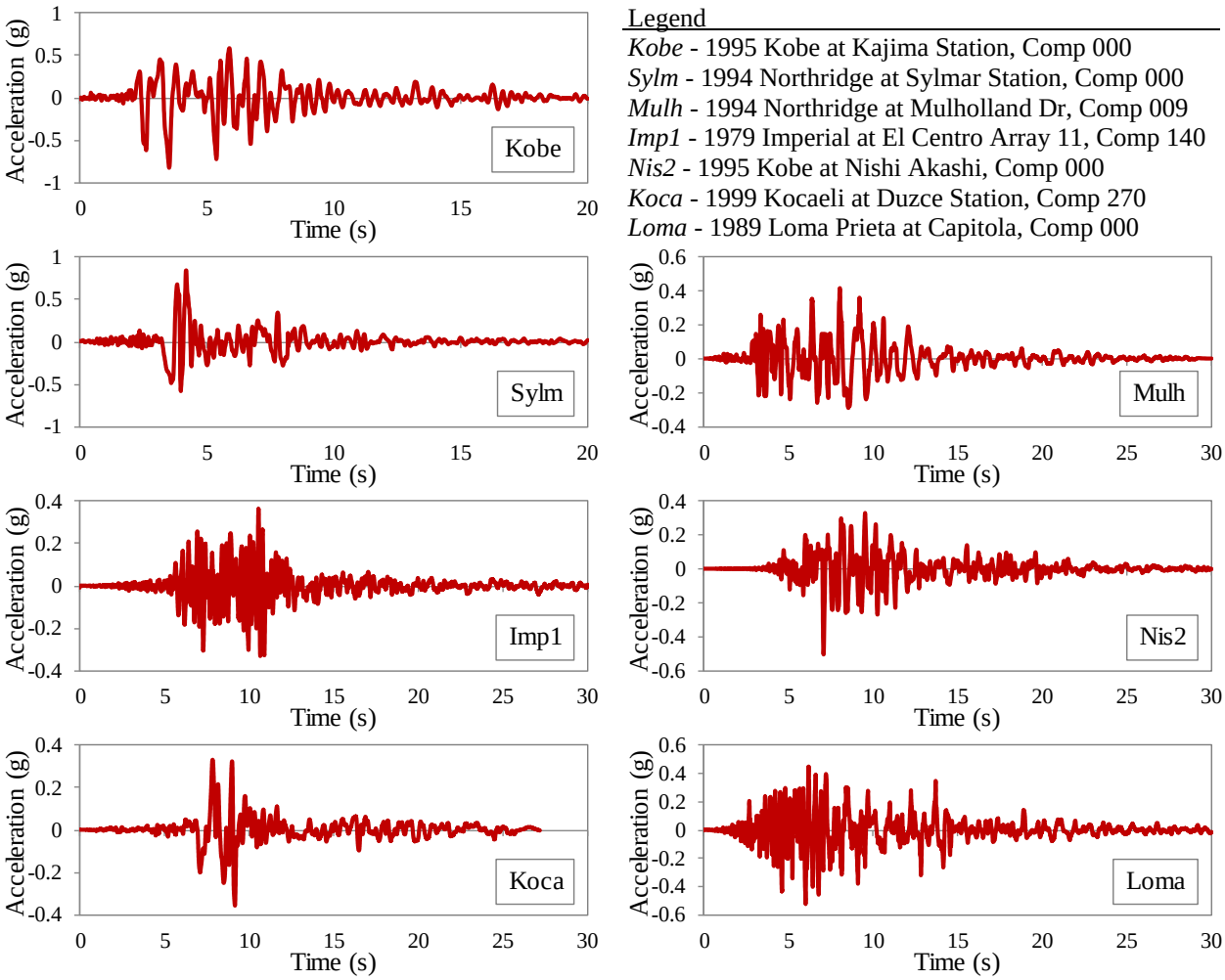

Figure 3: Investigated earthquake ground motions

First consider the *Kobe* earthquake with a scaling factor of 0.6, Fig. 4a shows the second floor displacement responses of the frame considering only geometric nonlinearity, and Fig. 4b shows the same responses considering both geometric and material nonlinearities. As shown in Fig. 4a

where only geometric nonlinearity is considered, all solution algorithms give similar responses, indicating that modeling parameters used in Table 2 for the PD, GS, SF, CR, and LD solution algorithms produce consistent results. However, as shown in Fig. 4b where both geometric and material nonlinearities are considered, the GS solution algorithm indicates collapse when all the other solution algorithms show minimum yielding with small amount of residual drifts. This suggests that there is a fundamental issue with the GS solution algorithm related to the coupling between geometric nonlinearity and material nonlinearity that causes numerical instability in the solution algorithm. Therefore, the GS solution algorithm is dropped from the subsequent study.

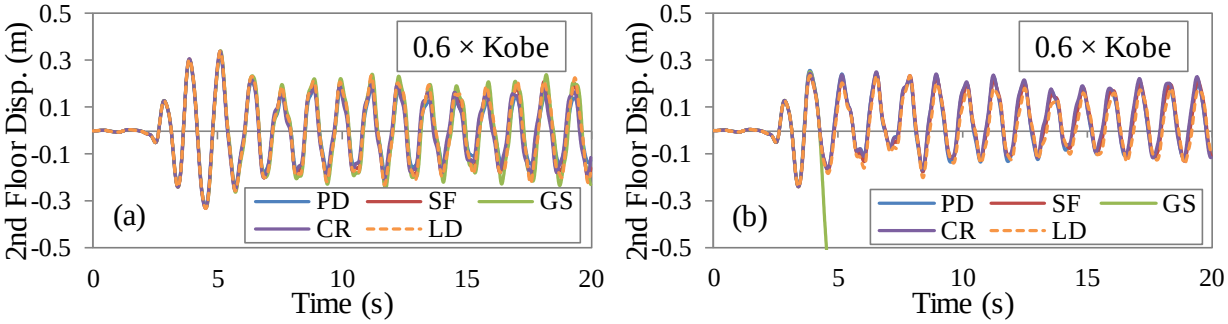

Figure 4: Displacement responses due to 0.6 × *Kobe* using different solution algorithms

The scaling factor continues to increase until collapse of the frame is observed, and Fig. 5 shows the roof displacement responses due to two different scaling factors of the *Kobe* earthquake. The left chart of Fig. 5 shows at least one solution algorithm indicates that the frame collapses at a scaling factor of 2.2. Using this scaling factor to indicate collapse, a slightly reduced scaling factor of 2.0 is used to cause the frame to reach the point of having large displacement but remains standing and stable, and the roof displacement responses due to this scaling factor is shown in the right chart of Fig. 5. The procedure is used here to define the scaling factor that causes near collapse. Corresponding to this level of displacements at near collapse (i.e., due to 2.0 × *Kobe*), the inter-story drifts of each floor is shown in Fig. 6. Table 3 summarizes the maximum inter-story drift of each floor for PD, CR, and SF and the corresponding percentage difference from the LD solution algorithm. In addition, the smallest percentage difference among each inter-story drift is highlighted in yellow for each row. Finally, the maximum inter-story drift among all eight floors using the LD solution algorithm is highlighted in orange.

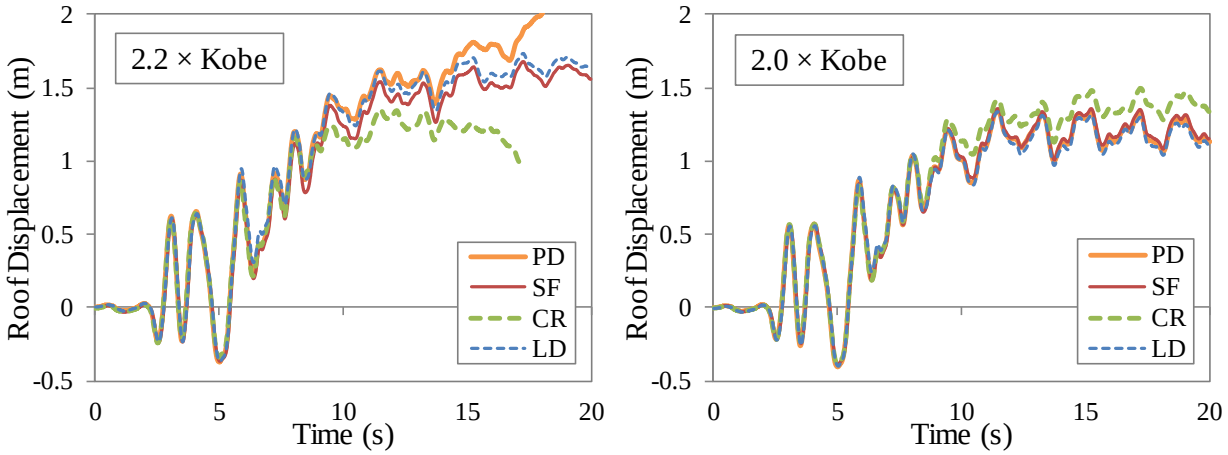

Figure 5: Roof responses of the eight-story frame at and near-collapse due to Kobe

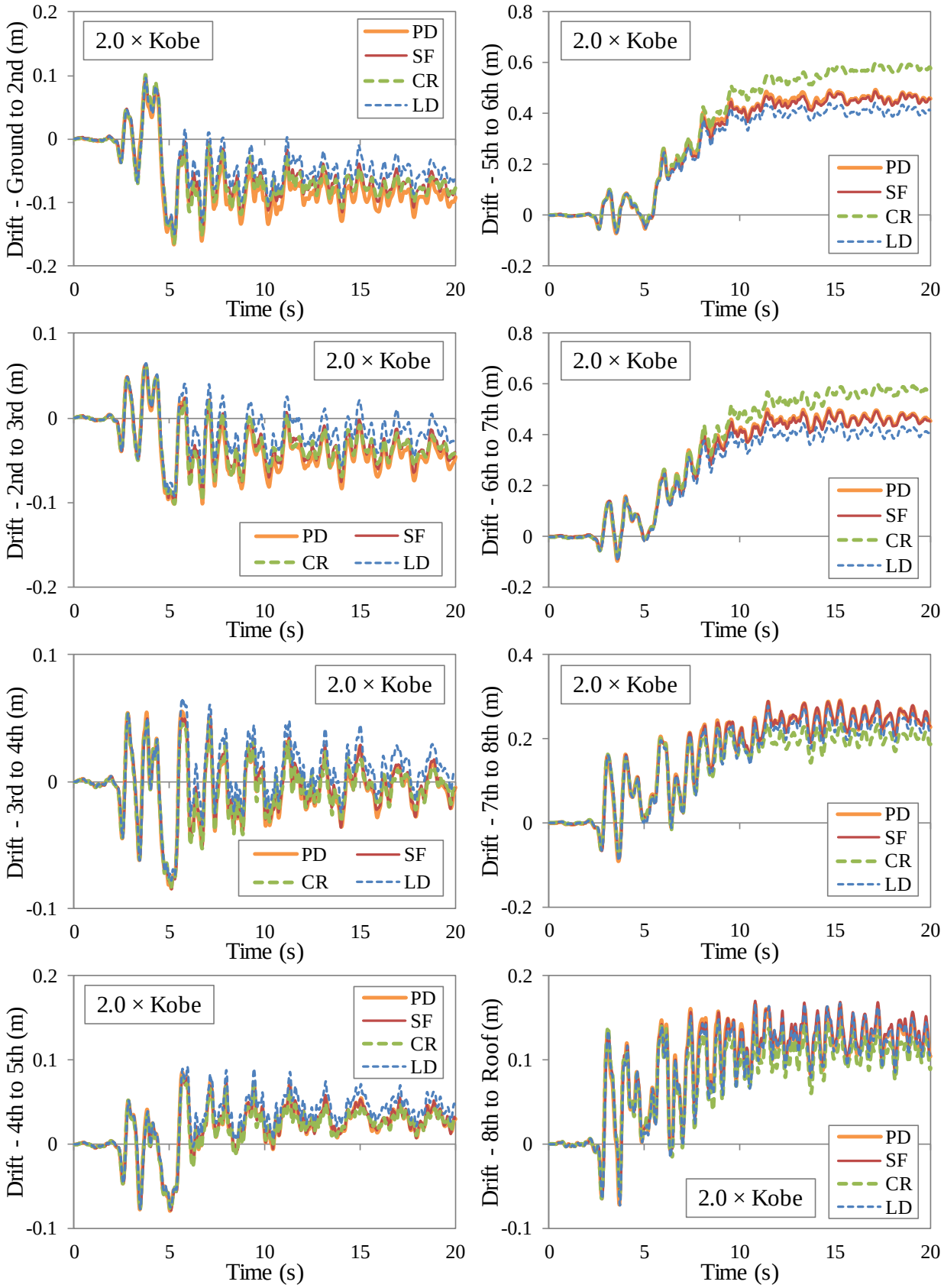

Figure 6: Inter-story drifts of the eight-story frame at near-collapse due to 2.0 × *Kobe* earthquake

Table 3: Maximum inter-story drift of 8-story frame due to 2.0 × *Kobe* earthquake at near-collapse

Location	LD	PD		CR		SF	
	Drift (m)	Drift (m)	% Diff	Drift (m)	% Diff	Drift (m)	% Diff
Ground – 2nd	0.149	0.167	12.2 %	0.164	9.8 %	0.155	3.7 %
2nd – 3rd	0.092	0.102	10.0 %	0.102	10.0 %	0.101	9.9 %
3rd – 4th	0.078	0.084	7.5 %	0.084	8.1 %	0.084	8.1 %
4th – 5th	0.092	0.086	6.7 %	0.080	12.7 %	0.081	11.8 %
5th – 6th	0.441	0.493	11.9 %	0.603	36.9 %	0.487	10.6 %
6th – 7th	0.455	0.506	11.3 %	0.604	32.7 %	0.496	9.1 %
7th – 8th	0.279	0.293	5.1 %	0.239	14.1 %	0.289	3.8 %
8th – Roof	0.167	0.166	0.4 %	0.149	10.5 %	0.171	2.5 %

Similar analyses are performed for the remaining six earthquake ground motions to identify the scaling factors that cause near collapse, and the results are shown in Figs. 7 to 12 with the maximum inter-story drifts at near collapse shown in Tables 4 to 9. It can be seen from the response history figures that the responses during the first few seconds among the four solution algorithms are nearly identical, indicating that the structural models are consistent.

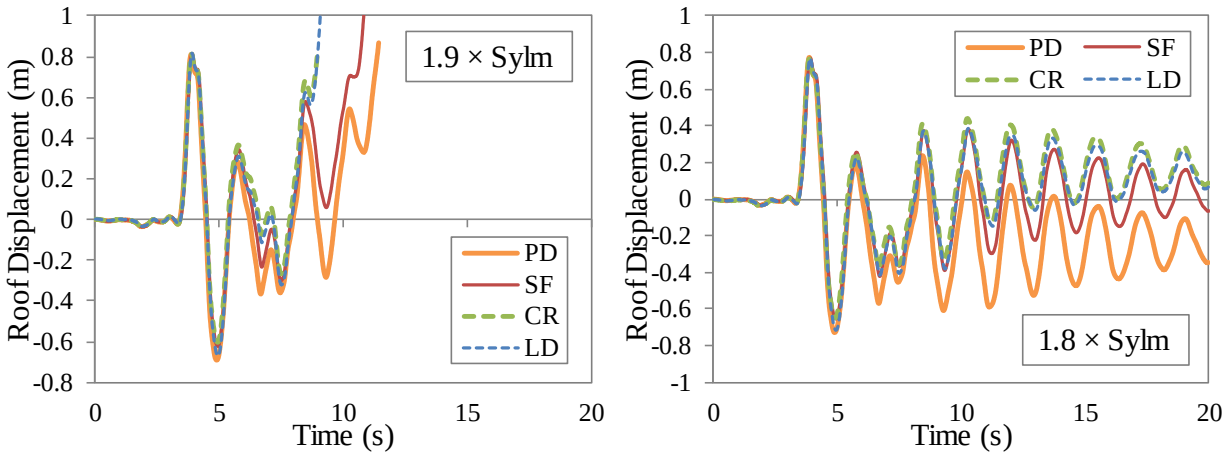

Figure 7: Roof responses of the eight-story frame at and near-collapse due to *Sylm* earthquake

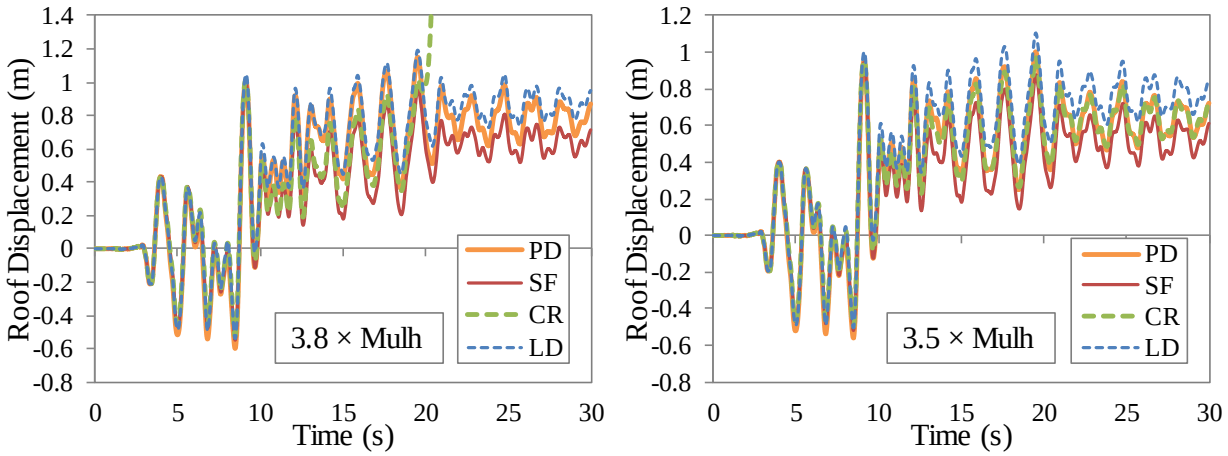

Figure 8: Roof responses of the eight-story frame at and near-collapse due to *Mulh* earthquake

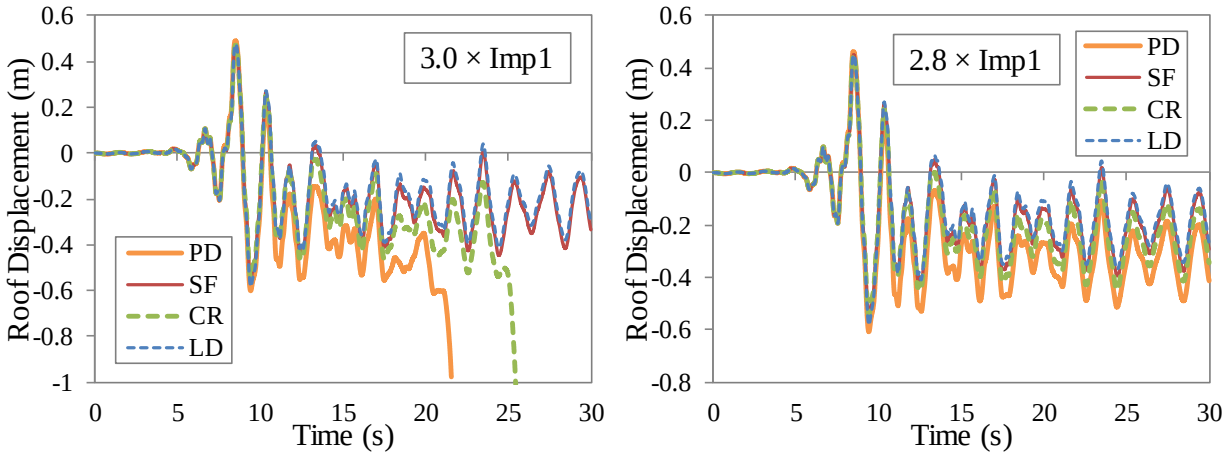

Figure 9: Roof responses of the eight-story frame at and near-collapse due to *Imp1* earthquake

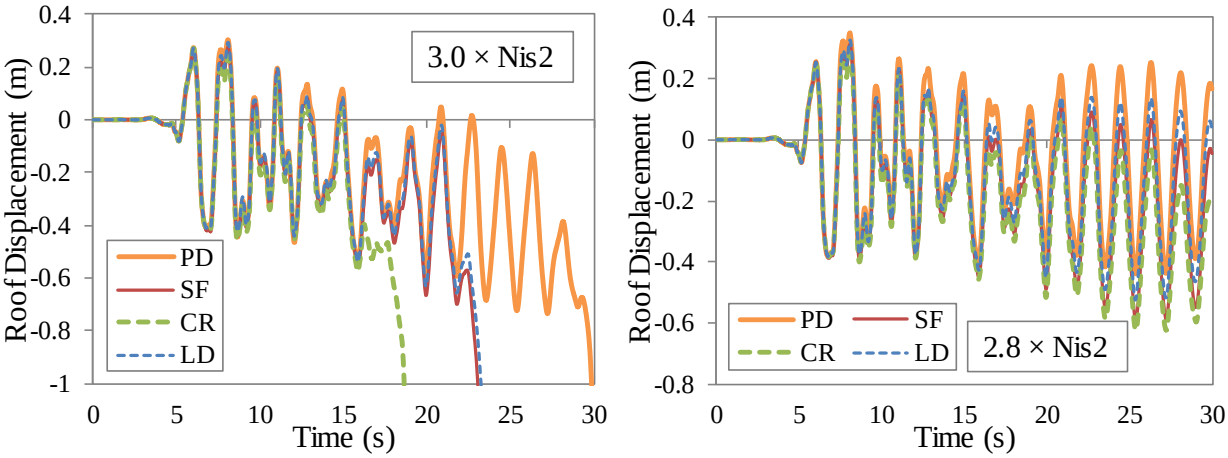

Figure 10: Roof responses of the eight-story frame at and near-collapse due to *Nis2* earthquake

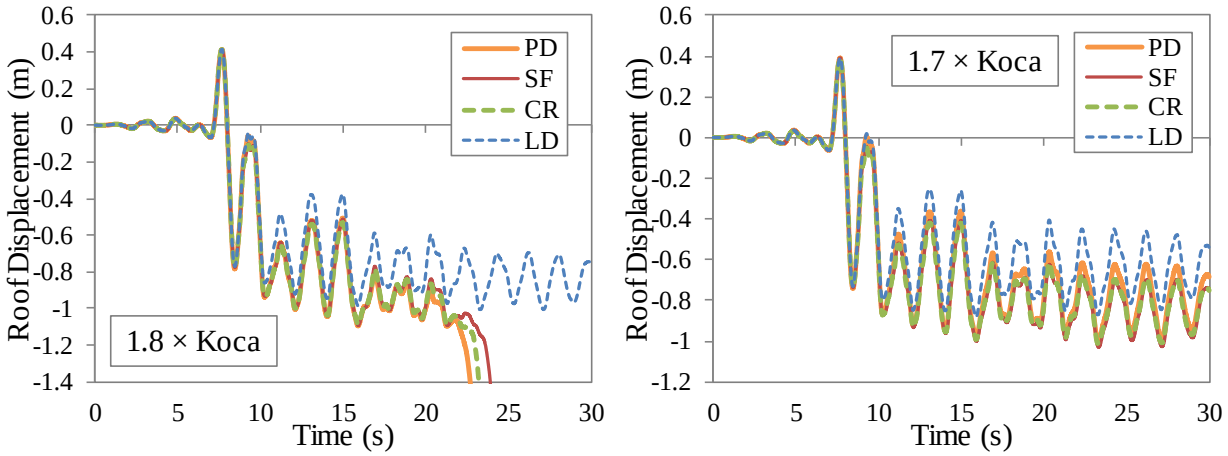

Figure 11: Roof responses of the eight-story frame at and near-collapse due to *Koca* earthquake

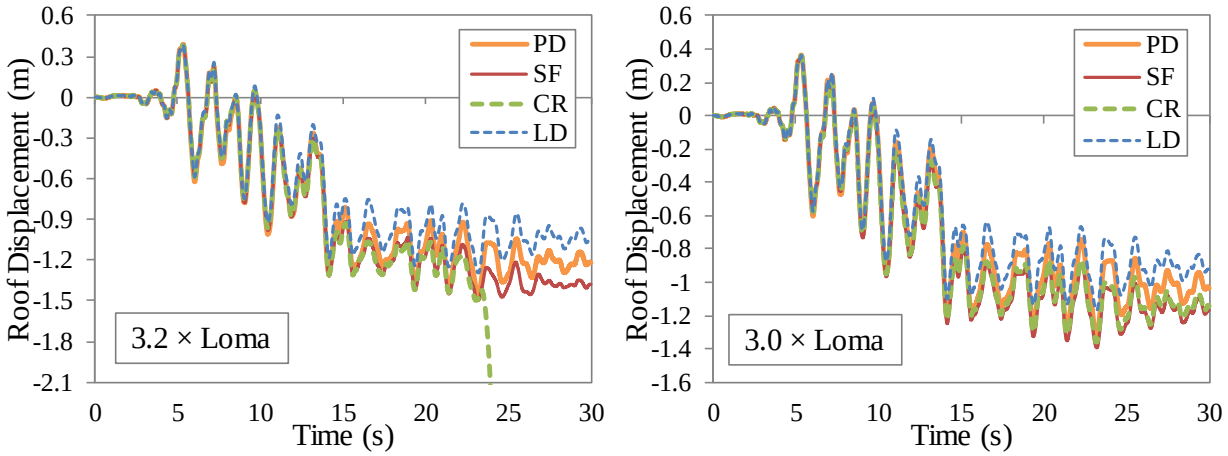

Figure 12: Roof responses of the eight-story frame at and near-collapse due to *Loma* earthquake

Table 4: Maximum inter-story drift of 8-story frame due to 1.8 × *Sylm* earthquake at near-collapse

Location	**LD**	**PD**		**CR**		**SF**	
	Drift (m)	Drift (m)	% Diff	Drift (m)	% Diff	Drift (m)	% Diff
Ground – 2nd	0.329	0.188	42.8 %	0.296	10.1 %	0.189	42.6 %
2nd – 3rd	0.142	0.134	5.4 %	0.142	0.2 %	0.138	2.6 %
3rd – 4th	0.104	0.108	3.8 %	0.105	1.3 %	0.111	6.8 %
4th – 5th	0.123	0.114	6.8 %	0.104	15.2 %	0.104	15.5 %
5th – 6th	0.159	0.129	18.9 %	0.139	12.4 %	0.127	19.7 %
6th – 7th	0.135	0.130	3.1 %	0.128	5.3 %	0.124	7.6 %
7th – 8th	0.104	0.106	2.0 %	0.102	2.0 %	0.104	0.2 %
8th – Roof	0.070	0.075	7.7 %	0.074	5.6 %	0.073	4.7 %

Table 5: Maximum inter-story drift of 8-story frame due to 3.5 × *Mulh* earthquake at near-collapse

Location	**LD**	**PD**		**CR**		**SF**	
	Drift (m)	Drift (m)	% Diff	Drift (m)	% Diff	Drift (m)	% Diff
Ground – 2nd	0.144	0.136	5.3 %	0.160	11.1 %	0.140	2.9 %
2nd – 3rd	0.099	0.105	6.6 %	0.103	4.6 %	0.101	1.9 %
3rd – 4th	0.101	0.101	0.2 %	0.093	8.0 %	0.093	7.5 %
4th – 5th	0.135	0.119	12.0 %	0.123	9.2 %	0.128	5.4 %
5th – 6th	0.253	0.261	3.1 %	0.240	4.9 %	0.229	9.4 %
6th – 7th	0.234	0.242	3.2 %	0.220	6.3 %	0.212	9.6 %
7th – 8th	0.173	0.190	9.6 %	0.154	11.2 %	0.151	12.9 %
8th – Roof	0.122	0.137	11.9 %	0.120	2.2 %	0.113	7.4 %

As shown in Figs. 5 and 7 to 12 for the responses at both collapse and near collapse, the amplitudes and frequencies of oscillations for post-yield responses among the four solution algorithms are about the same, but that the centers of oscillation (i.e., residual drifts) have been shifted due to yielding. This is particularly evident in Fig. 10 where significant differences for the center-of-oscillation on the right chart is observed among the solution algorithms toward the end of the 30-second analysis. This suggests that the amplitudes and frequencies of oscillations have been captured consistently by the "dynamic" solvers among the four solution algorithms,

but the "nonlinear" solvers among each algorithm are unable to capture consistent residual drifts that result in different offsets for the center-of-oscillation. This observation highlights the differences in how the coupling between geometric nonlinearity and material nonlinearity in the nonlinear solver among each algorithm affects the simulated responses. Based on the observations of residual drifts in the figures and using LD results as the comparison standard, SF matches LD very well for *Kobe* (Fig. 5), *Imp1* (Fig. 9), and *Nis2* (Fig. 10), while CR matches LD very well for *Sylm* (Fig. 7). PD consistently produces different residual drifts from LD, but it matches LD the best for *Mulh* (Fig. 8) and *Loma* (Fig. 12). Finally, none of the three algorithms matches LD for *Koca* (Fig. 11). This suggests that SF is more suitable for capturing large displacement responses among the solution algorithms in terms of residual drifts.

Table 6: Maximum inter-story drift of 8-story frame due to 2.8 × *Imp1* earthquake at near-collapse

Location	**LD**	**PD**		**CR**		**SF**	
	Drift (m)	Drift (m)	% Diff	Drift (m)	% Diff	Drift (m)	% Diff
Ground – 2nd	0.207	0.297	43.7 %	0.279	35.0 %	0.235	13.7 %
2nd – 3rd	0.123	0.152	23.6 %	0.138	11.9 %	0.131	6.8 %
3rd – 4th	0.099	0.113	13.8 %	0.103	4.1 %	0.103	3.7 %
4th – 5th	0.078	0.078	0.9 %	0.070	10.5 %	0.071	9.1 %
5th – 6th	0.099	0.095	3.6 %	0.104	5.4 %	0.102	3.5 %
6th – 7th	0.120	0.122	2.0 %	0.124	3.4 %	0.123	3.0 %
7th – 8th	0.097	0.108	10.7 %	0.106	8.8 %	0.106	9.0 %
8th – Roof	0.077	0.085	10.8 %	0.081	4.6 %	0.080	4.0 %

Table 7: Maximum inter-story drift of 8-story frame due to 2.8 × *Nis2* earthquake at near-collapse

Location	**LD**	**PD**		**CR**		**SF**	
	Drift (m)	Drift (m)	% Diff	Drift (m)	% Diff	Drift (m)	% Diff
Ground – 2nd	0.180	0.138	23.6 %	0.311	72.8 %	0.214	18.8 %
2nd – 3rd	0.097	0.078	19.6 %	0.127	31.2 %	0.125	29.6 %
3rd – 4th	0.069	0.067	3.1 %	0.074	6.3 %	0.076	9.2 %
4th – 5th	0.057	0.059	4.7 %	0.056	1.4 %	0.057	0.5 %
5th – 6th	0.073	0.076	4.1 %	0.074	2.0 %	0.073	0.6 %
6th – 7th	0.098	0.102	3.7 %	0.097	1.0 %	0.097	1.0 %
7th – 8th	0.117	0.122	4.4 %	0.114	2.0 %	0.113	2.8 %
8th – Roof	0.093	0.096	3.0 %	0.094	0.3 %	0.094	1.1 %

Table 8: Maximum inter-story drift of 8-story frame due to 1.7 × *Koca* earthquake at near-collapse

Location	**LD**	**PD**		**CR**		**SF**	
	Drift (m)	Drift (m)	% Diff	Drift (m)	% Diff	Drift (m)	% Diff
Ground – 2nd	0.256	0.327	27.8 %	0.334	30.8 %	0.334	30.6 %
2nd – 3rd	0.159	0.192	20.4 %	0.191	19.6 %	0.197	23.4 %
3rd – 4th	0.125	0.133	6.5 %	0.137	10.0 %	0.140	11.8 %
4th – 5th	0.102	0.105	2.3 %	0.106	3.8 %	0.108	5.9 %
5th – 6th	0.108	0.113	4.4 %	0.115	6.7 %	0.117	8.3 %
6th – 7th	0.108	0.113	4.6 %	0.115	7.2 %	0.117	8.4 %
7th – 8th	0.103	0.109	5.7 %	0.109	6.5 %	0.109	6.3 %
8th – Roof	0.071	0.074	5.3 %	0.075	5.5 %	0.074	4.9 %

Table 9: Maximum inter-story drift of 8-story frame due to 3.0 × *Loma* earthquake at near-collapse

Location	**LD**	**PD**		**CR**		**SF**	
	Drift (m)	Drift (m)	% Diff	Drift (m)	% Diff	Drift (m)	% Diff
Ground – 2nd	0.110	0.160	46.1 %	0.226	106.2 %	0.208	89.6 %
2nd – 3rd	0.093	0.130	39.5 %	0.160	72.3 %	0.157	69.4 %
3rd – 4th	0.110	0.127	15.1 %	0.139	25.9 %	0.142	28.3 %
4th – 5th	0.118	0.140	18.6 %	0.137	15.9 %	0.142	20.3 %
5th – 6th	0.252	0.241	4.4 %	0.241	4.1 %	0.249	1.2 %
6th – 7th	0.263	0.251	4.6 %	0.247	6.0 %	0.259	1.5 %
7th – 8th	0.219	0.220	0.7 %	0.198	9.4 %	0.211	3.4 %
8th – Roof	0.142	0.151	6.0 %	0.124	12.6 %	0.135	4.7 %

Besides residual drift, another method of comparing the solution algorithms is by looking at the maximum inter-story drifts. Tables 3 to 9 summarize the PD, CR, and SF maximum inter-story drifts of each floor at near-collapse of the 8-story frame and the percentage differences from those computed by the LD solution algorithm. Here, the LD results are again used as the comparison standard. It can be seen from these tables that both PD and SF record the smallest percentage difference (i.e., counting the number of highlighted yellow cells) 23 times, and CR records the smallest percentage difference 11 times. This suggests that both PD and SF are more suitable for capturing large displacement responses in terms of counting the number of percentage differences. A more objective way of comparing Tables 3 to 9 is via uncertainties as shown in Table 10, where the means and standard deviations of the percentage differences are evaluated at near-collapse of the frame. This table shows the PD solution algorithm simulates responses that have only 10.6 % differences from the LD responses with a standard deviation of 11.0 %, This is followed by the SF solution algorithm with a mean of 11.6 % and finally by CR with a mean of 14.1 %. This suggests that the PD solution algorithm simulates the maximum inter-story drifts with the least uncertainty.

Table 10: Uncertainties in percentage differences of maximum inter-story drifts

	PD	**CR**	**SF**
Mean	10.6 %	14.1 %	11.6 %
Standard Deviation	11.0 %	19.1 %	15.7 %

A careful consideration of the values in Tables 3 to 9 indicates that there can be biases toward maximum inter-story drifts that are not important. For example, as shown in Table 9 for the maximum inter-story drift between the ground and second floor, LD predicts only a drift of 0.110 m, while the maximum inter-story drift occurs between the sixth and seventh floors at 0.263 m. The CR result shows that predicting the maximum inter-story drift between the ground and second floor gives a percentage difference of over 100 %, while predicting the maximum inter-story drift between sixth and seventh floor gives a percentage difference of only 6.0 %. This means that computing the mean using data points with such a high percentage difference but at some unimportant locations may not accurately reflect the precision of the solution algorithms. Therefore, an alternate approach is here considered to look at only the floor having the largest value of maximum inter-story drifts for the LD responses (i.e., the rows with LD responses highlighted in orange). These largest values are extracted from Tables 3 to 9 for each

earthquake and summarized in Table 11. The corresponding means and standard deviations of the percentage differences are also calculated and shown in the table. Results show the SF solution algorithm simulates responses that have only 17.9 % differences from the LD responses with a standard deviation of 13.1 %, This is followed by the PD solution algorithm with a mean of 22.4 % and finally by CR with a mean of 27.5 %. This suggests that the SF solution algorithm simulates the largest values of maximum inter-story drifts with the least uncertainty, which is where these drifts matter most.

Table 11: Maximum inter-story drift of 8-story frame at near-collapse

Earthquake/ (Inter-story)	**LD**	**PD**		**CR**		**SF**	
	Drift (m)	Drift (m)	% Diff	Drift (m)	% Diff	Drift (m)	% Diff
2.0 × *Kobe* (6-7)	0.455	0.506	11.3 %	0.604	32.7 %	0.496	9.1 %
1.8 × *Sylm* (G-2)	0.329	0.188	42.8 %	0.296	10.1 %	0.189	42.6 %
3.5 × *Mulh* (5-6)	0.253	0.261	3.1 %	0.240	4.9 %	0.229	9.4 %
2.8 × *Imp1* (G-2)	0.207	0.297	43.7 %	0.279	35.0 %	0.235	13.7 %
2.8 × *Nis2* (G-2)	0.180	0.138	23.6 %	0.311	72.8 %	0.214	18.8 %
1.7 × *Koca* (G-2)	0.256	0.327	27.8 %	0.334	30.8 %	0.334	30.6 %
3.0 × *Loma* (6-7)	0.263	0.251	4.6 %	0.247	6.0 %	0.259	1.5 %
Mean			22.4 %		27.5 %		17.9 %
Standard Deviation			15.6 %		22.1 %		13.1 %

5. Conclusions

Different small displacement formulations make different assumptions in their solution algorithms to produce nonlinear structural dynamic responses. In this study, different forms of geometric nonlinearity have been investigated by selecting four small-displacement-based software packages using P-Delta stiffness formulation (PD), geometric stiffness (GS), corotation formulation (CR), and stability functions formulation (SF). While SF, GS, and PD are similar in the derivation based on Bernoulli-Euler beam theory but use different approximations for equilibrium in the deformed state, CR considers rigid body motion in its formulation while writing equilibrium according to its rigid-body state. These differences in geometric nonlinearity are coupled with each inherent material nonlinearity assumptions, producing nonlinear solvers that are quite different among each small-displacement-based solution algorithm. This results in output responses that are quite different and often quite difficult to track. To study the differences, a consistent 8-story steel moment-resisting frame model has been developed using PD, GS, CR, and SF, and the output inter-story drift responses due to seven earthquake ground motions are compared with those obtained from LD, a large-displacement-based finite element analysis software package that is assumed to produce the most precise responses for the given model. Comparison of responses shows that consistency is obtained in the amplitudes and frequencies of oscillations among the solution algorithms except for GS, suggesting that the dynamic solvers among each solution algorithm are reasonably consistent. The inconsistency occurs in the center-of-oscillations (i.e., residual drifts) predicted by each solution algorithm, suggesting that the nonlinear solvers for handling coupled material and geometric nonlinearities are the source of inconsistency.

Uncertainties due to the inconsistency among the small-displacement-based PD, CR, and SF solution algorithms are also quantified. Based on comparisons with LD responses, results show

the mean percentage differences range from 10 % to 30 % at near-collapse based on the use of seven earthquake ground motions. Between the small-displacement-based solution algorithms, results show that SF has better performance based on residual drifts, while PD has better performance based on maximum inter-story drifts and SF has better performance based on the largest values of maximum inter-story drifts. From this study, can small-displacement-based solution algorithms be used to predict large displacement responses at near collapse? The answer should be 'yes' because both small-displacement-based and large-displacement-based solution algorithms produce global dynamic responses with similar vibration characteristics. Differences lie in how each solution algorithm handles material nonlinearity, particularly during the transition from elastic to inelastic response or vice versa. This suggests that further research on improving the material nonlinearity models and the associated solution algorithms is necessary.

References

Arabzadeh, H., Galal, K. (2017). "Seismic collapse risk assessment and FRP retrofitting of RC coupled C-shaped core walls using the FEMA P695 methodology." *Journal of Structural Engineering ASCE*, 143 (9) 04017096.

Bazant, Z.P., Cedolin, L. (2003). *Stability of Structures*, Dover Publication, New York, USA.

Belytschko, T., Hsieh, B.J. (1973). "Nonlinear transient finite element analysis with convected coordinates." *International Journal for Numerical Methods in Engineering*, 7 (3) 255-271.

Belytschko, T., Liu, W.K. (2014). *Nonlinear Finite Elements for Continua and Structures*, 2nd Edition, John Wiley & Sons, Chichester, UK.

Domizio, M., Ambrosini, D., Curadelli, O. (2015). "Experimental and numerical analysis to collapse of a framed structure subjected to seismic loading." *Engineering Structures*, 82, 22-32.

Eads, L., Miranda, E., Krawinkler, H., Lignos, D.G. (2013). "An efficient method for estimating the collapse risk of structures in seismic regions." *Earthquake Engineering and Structural Dynamics*, 42 (1) 25-41.

Fathieh, A., Mercan, O. (2016). "Seismic evaluation of modular steel buildings." *Engineering Structures*, 122, 83-92.

Grigorian, M., Grigorian, C.E. (2012). "Lateral displacements of moment frames at incipient collapse." *Engineering Structures*, 44, 174-185.

Guo, T., Song, L.L., Zhang, G.D. (2015). "Numerical simulation and seismic fragility analysis of a self-centering steel MRF with web friction devices." *Journal of Earthquake Engineering*, 19 (5) 731-751.

Li, G., Wong, K.K.F. (2014). *Theory of Nonlinear Structural Analysis: The Force Analogy Method for Earthquake Engineering*, John Wiley & Sons, Singapore.

Lignos, D.G., Krawinkler, H., Whittaker, A.S. (2011). "Prediction and validation of sidesway collapse of two scale models of a 4-story steel moment frame." *Earthquake Engineering and Structural Dynamics*, 40 (7) 807-825.

Mulas, M.G., Martinelli, P. (2017). "Numerical simulation of the partial seismic collapse of a 1960s RC building." *Journal of Performance of Constructed Facilities ASCE*, 31 (6) 04017111.

Murray, J.A., Sasani, M. (2016). "Near-collapse response of existing RC building under severe pulse-type ground motion using hybrid simulation." *Earthquake Engineering and Structural Dynamics*, 45 (7) 1109-1127.

Pang, W.C., Shirazi, S.M.H. (2013). "Corotational model for cyclic analysis of light-frame wood shear walls and diaphragms." *Journal of Structural Engineering ASCE*, 139 (8) 1303-1317.

Powell, G.H. (2010). *Modeling for Structural Analysis: Behavior and Basics*, Computers and Structures, California USA.

Reddy, J.N. (2015). *An Introduction to Nonlinear Finite Element Analysis*, 2nd Edition, Oxford University Press, Oxford, UK.

Sivaselvan, M.V., Reinhorn, A.M. (2002). "Collapse analysis: large inelastic deformations analysis of planar frames." *Journal of Structural Engineering ASCE*, 128 (12) 1575-1583.

Timoshenko, S.P., Gere, J.M. (1961). *Theory of Elastic Stability*, 2nd Edition, McGraw Hill, New York, USA.

Tirca, L., Chen, L., Tremblay, R. (2015). "Assessing collapse safety of CBF buildings subjected to crustal and subduction earthquake." *Journal of Constructional Steel Research*, 115, 47-61.

Wang, S.S., Lai, J.W., Schoettler, M.J., Mahin, S.A. (2017). "Seismic assessment of existing tall buildings: a case study of a 35-story steel building with pre-Northridge connection." *Engineering Structures*, 141, 624-633.

Wilson, E. (2010). *Static and Dynamic Analysis of Structures: A Physical Approach with Emphasis on Earthquake Engineering*, 4th Edition, Computer and Structures, California, USA.